Supporting Information

Site-Selective Growth of Crystalline Ceria with Oxygen Vacancies on Gold Nanocrystals for Near-Infrared Nitrogen Photofixation

Henglei Jia,[†] Aoxuan Du,[†] Han Zhang,[‡] Jianhua Yang,[‡] Ruibin Jiang,*,[§] Jianfang Wang,*,[‡] Chun-yang Zhang*,[†]

[†]College of Chemistry, Chemical Engineering and Materials Science, Collaborative Innovation Center of Functionalized Probes for Chemical Imaging in Universities of Shandong, Key Laboratory of Molecular and Nano Probes, Ministry of Education, Shandong Provincial Key Laboratory of Clean Production of Fine Chemicals, Shandong Normal University, Jinan 250014, China

[‡]Department of Physics, The Chinese University of Hong Kong, Shatin, Hong Kong SAR, China

[§]Shaanxi Engineering Lab for Advanced Energy Technology, School of Materials Science and Engineering, Shaanxi Normal University, Xi'an 710119, China

Contents

Supporting Experimental Section

Chemicals. Sodium borohydride (NaBH$_4$, 99%), hexadecyltrimethylammonium bromide (CTAB, for molecular biology, $\geq$ 99.0%), silver nitrate (AgNO$_3$, $\geq$ 99.0%), L-ascorbic acid (AA, $\geq$ 99.0%), cerium (III) acetate hydrate (Ce(AC)$_3$·xH$_2$O, 99.9%), and 9, 10-anthracenediyl-bis (methylene) dimalonic acid (ABDA, $\geq$ 90%) were purchased from Sigma-Aldrich. Tetrachloroauric (III) acid tetrahydrate (HAuCl$_4$·4H$_2$O), hydrochloric acid (HCl, ~36.0–38.0 w%), and methanol (CH$_3$OH, $\geq$ 99.5%) were obtained from Sinopharm Chemical Reagent. Cerium nitrate hexahydrate (Ce(NO$_3$)$_3$·6H$_2$O, $\geq$ 99.5%), potassium sodium tartrate tetrahydrate (C$_4$H$_4$O$_6$KNa·4H$_2$O, 99%), salicylic acid (C$_6$H$_4$(OH)COOH, $\geq$ 99.0%), sodium hypochlorite solution (NaClO, available chlorine $\geq$ 5.0%) and ammonium chloride (NH$_4$Cl, PT) were purchased from Aladdin Reagent. Potassium tetrachloroplatinate (II) (K$_2$PtCl$_4$), chloroplatinic acid hexahydrate (H$_2$PtCl$_6$·6H$_2$O), and palladium (II) chloride (PdCl$_2$) were obtained from Shenyang Research Institute of Nonferrous Metals. Sodium nitroferricyanide (III) dihydrate (Na$_2$[Fe(CN)$_5$NO]·2H$_2$O) was obtained from Macklin. Deionized (DI) water with a resistivity of 18.2 MΩ·cm was used in all experiments.

Growth of the Au nanorods (NRs). The starting Au NRs were prepared following a seed-mediated growth method with some modifications.[1,2] Specifically, the seed solution was prepared by injecting a freshly prepared, ice-cold NaBH$_4$ solution (10 mM, 600 μL) into a mixture containing HAuCl$_4$ (10 mM, 250 μL) and CTAB (0.1 M, 9.75 mL), followed by rapid inversion for 2 min. The resultant seed solution was kept at room temperature for 2 h prior to use. The growth solution was prepared by the sequential addition of HAuCl$_4$ (10 mM, 2 mL), AgNO$_3$ (10 mM, 400 μL), and HCl (1 M, 800 μL) into CTAB solution (0.1 M, 40 mL), followed by the addition of a freshly prepared AA solution (0.1 M, 320 μL). Once the resultant solution turned colorless, the seed solution (10, 30, and 100 μL for three Au NR samples, respectively) was then injected into the growth solution and mixed by inversion for 2 min. The resultant solution was kept undisturbed for at least 6 h.

Growth of the Au/end-CeO$_2$ nanostructures. Typically, the as-grown Au NR solution (10 mL) was collected by centrifugation and washing with DI water (30 mL) to remove the excess surfactant. The Au NRs were then

redispersed into CTAB solution (0.1 mM, 5 mL) in a 15-mL centrifuge tube. The K_2PtCl_4 solution (0.1 mM, 200 μL) was subsequently added into the Au NR solution under gentle shaking. The resultant solution was kept at room temperature for 2 min to allow for the adsorption of $PtCl_4^{2-}$ on the Au NRs. A freshly prepared $Ce(AC)_3$ solution (10 mM, 500 μL) and DI water (4.3 mL) were sequentially added into the Au NR solution under gentle shaking. The overall volume of the obtained solution was 10 mL with the CTAB concentration of 50 μM. The resultant solution was placed in an oven set at 100 °C for 1 h to produce the Au/end-CeO_2 nanostructures. The product was washed by centrifugation and redispersed in DI water (10 mL) for further use.

Near-infrared (NIR) photocatalytic nitrogen fixation. The photocatalytic nitrogen fixation reaction was conducted in a 1-cm cuvette (4.2 mL). Methanol was used as the hole scavenger. For a typical reaction, the catalyst (1.3 mg) was dispersed into a mixture solution containing methanol and water (2:8, v/v, 1 mL) in a 1-cm cuvette. The mixture was bubbled with a constant high-purity N_2 (30 mL·min^{-1}) at a pressure of 1 atm for 10 min to remove dissolved air prior to the illumination. A semiconductor diode laser (808 nm) was employed for the NIR illumination at an optical power of 1.6 W. The optical power density was ~8 W·cm^{-2} at a spot diameter of 5 mm. The 808-nm laser instead of a broadband light source was used for illumination because (1) plasmon-induced NIR N_2 photofixation performance of the Au-end CeO_2 sample can be clearly demonstrated under its plasmon excitation, and (2) the longitudinal plasmon wavelength of Au NRs is synthetically tuned from visible to NIR regions by simple tailoring their aspect ratios.[3] Notably, the N_2 photofixation activity will be enhanced by extending the light absorption across the entire NIR range using the mixture of Au-end CeO_2 samples with different aspect ratios.[4] The laser beam was introduced perpendicular to the side surface into the solution. The solution was bubbled with N_2 (5 mL·min^{-1}) for the entire photocatalytic process. After 2-h illumination, the catalyst was recovered by centrifugation, and the product ammonia in the supernatant was determined with the indophenol-blue method.[4,5] Each experiment was repeated three times to obtain the average value and the standard deviation.

Detection of singlet oxygen ($^1O_2$). The generation of singlet oxygen was monitored using the probe molecule ABDA. The ABDA can be oxidized by $^1O_2$ to produce an endoperoxide, resulting in the decrease of the absorption intensity. For the detection of $^1O_2$, the catalyst (0.26 mg) was dispersed into ABDA solution (0.1 mM, 4 mL) in a cuvette (4.2 mL) with 1-cm path length. The mixture solution was stirred for more than 4 h in dark to reach the adsorption equilibrium prior to experiments. The same laser as the nitrogen fixation reaction was employed for the NIR illumination. For each 15-min illumination, 0.5 mL of solution was extracted and centrifuged to remove the catalytic nanoparticles. The supernatant was subjected to the absorption measurement.

Mechanism of the selective nucleation at the ends of Au NRs. For the Au NRs prepared with CTAB as the surfactant, the CTAB chains at the ends are sparser than those at the side of Au NRs, which has been confirmed by previous researches.[6–10] Two possible mechanisms have been proposed to explain this phenomenon. One is from the perspective of the curvature of the surface, named as Mechanism I.[7,8] The other is based on the consideration of the different facets exposed at the ends and the side of the Au NRs, named as Mechanism II.[9,10] In Mechanism I, it is generally believed that the curvature at the ends is larger than that at the side surface of Au NRs.[7,8] Although the use of the curvature to depict the geometry difference between the side and ends of the Au NRs is imprecise because the cylindrical surface is curved in one direction, the spherical surface at the ends is curved in two directions, and it can effectively reflect the geometrical difference. At comparable curvature radii, the spatial density of the molecular chains of the surfactant at the spherical surface is smaller than that at the cylindrical surface.[7] This mechanism has been employed in many previous researches to explain the preferential growth and the oxidation of Au NRs at the ends[11,12] and the easier access of molecules (titania and silica precursors).[7,8] In Mechanism II, it is believed that Au NRs are enclosed with the {100} and {110} facets at the side surface and the {111} facets at the ends,[13–16] and the surfactant molecules preferentially bind to the side {110} facets[14,15] and {100} facets.[9,16] Such a preferential binding results in sparser CTAB molecules at the ends than at the side of Au NRs and thereby leads to the selective growth of the second material on the ends of Au NRs. This mechanism has been used to explain the preferential adsorption of molecules like thiol molecules and Pt species on the ends.[9,10,17]

So far, it still remains elusive to tell which mechanism plays a dominant role. Fortunately, both mechanisms give the same result that the density of CTAB molecules at the ends is smaller than that at the side of Au NRs, which causes the preferential adsorption of $PtCl_4^{2-}$ on the ends of Au NRs. In addition, it is well known that the tips of Au NRs are composed of the {111} facets,[13,18] which is favorable for the deposition of Pt nanoparticles due to the similar lattice constant to the Pt {111} facets.[19]

Based on the above discussion, we proposed a possible mechanism for the preferential nucleation of Pt on the ends of Au NRs. Because the CTAB bilayers are less compact at the ends of Au NRs than that on the side surface due to the crystal structure and the curvature difference, $PtCl_4^{2-}$ ions preferentially adsorb at two ends of the Au NRs with a smaller steric hindrance. In addition, the similar lattice constant of the Pt {111} facets with the Au {111} facets at the ends is favorable for the deposition of Pt nanoparticles. The preferential nucleation of Pt subsequently guides the selective nucleation and growth of CeO_2.

Characterization. Low-magnification transmission electron microscopy (TEM) imaging was carried out on an HT7700 electron microscope at 100 kV. High-resolution transmission electron microscopy (HRTEM), high-angle annular dark-field scanning transmission electron microscopy (HAADF-STEM) imaging and elemental mapping were conducted on a FEI Tecani F20 microscopy equipped with an Oxford energy-dispersive X-ray analysis system. X-ray photoelectron spectroscopy (XPS) spectra were measured on a Thermo Scientific ESCALAB 250Xi spectrometer equipped with an Al Kα X-ray source ($h\nu$ = 1486.6 eV). The extinction spectra of the solution samples were taken on a Hitachi U-3900 ultraviolet/visible/NIR spectrophotometer with 1.0 cm quartz cuvettes. X-ray diffraction (XRD) patterns were measured on a Rigaku Dmax 2500 PC diffractometer equipped with Cu Kα radiation. Inductively coupled plasma optical emission spectroscopy (ICP-OES) was taken out on a PerkinElmer Optima 7300 DV system. Low-temperature electron paramagnetic resonance (EPR) spectrum was measured on a Bruker A300 at 77 K.

Supporting Figures
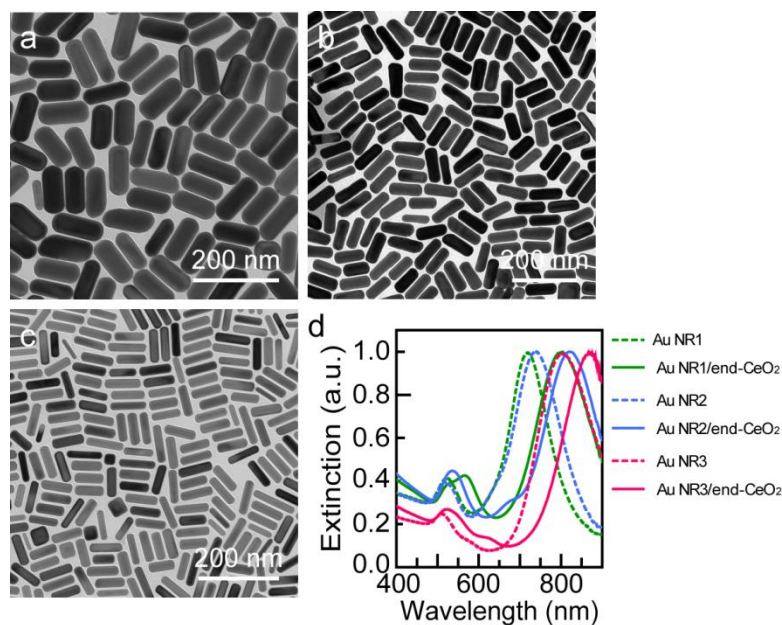
Figure S1. (a–c) TEM images of three starting Au NR samples. (d) Extinction spectra of three Au NR samples before (dashed lines) and after (solid lines) the selective coating of CeO_2. The average diameters of the Au NRs are 40.6 ± 3.1 nm, 31.6 ± 2.3 nm, and 18.3 ± 1.4 nm, and their longitudinal plasmon resonance wavelengths are 718 nm, 738 nm, and 803 nm, respectively.
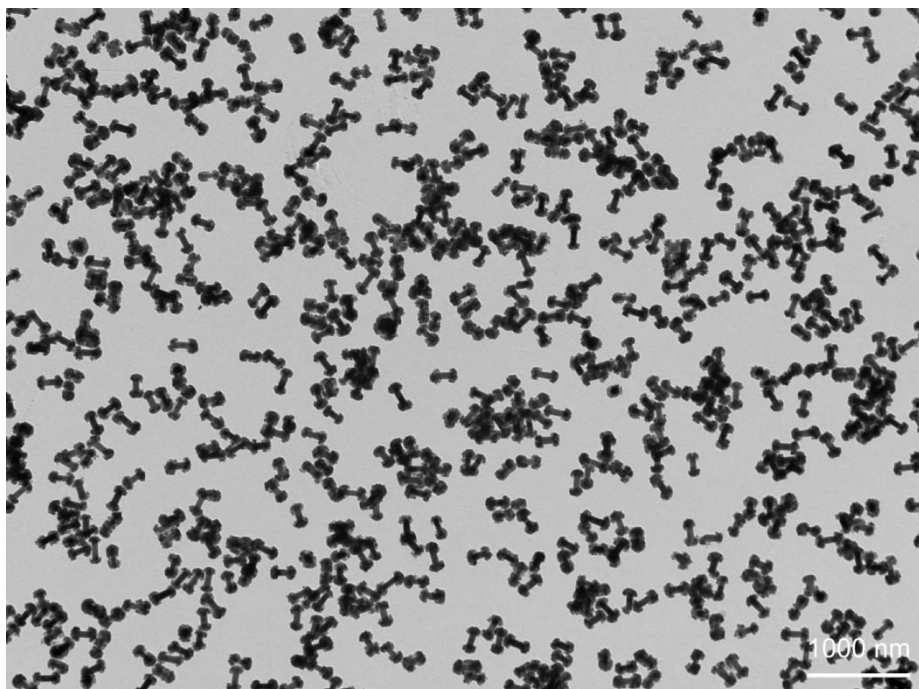
Figure S2. Representative TEM image of the Au NR2/end-CeO$_2$ nanostructures at a low magnification.
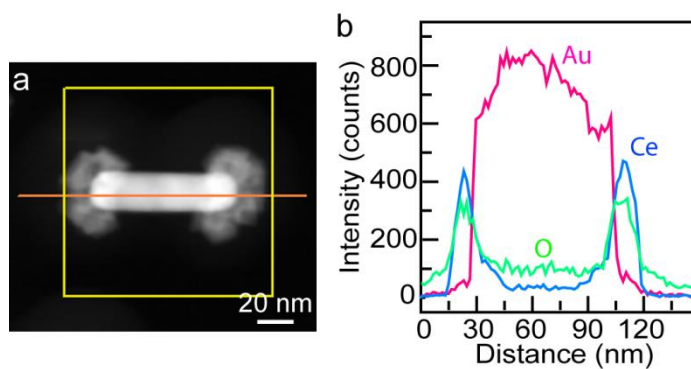
Figure S3. Elemental profiles of a single Au/end-CeO$_2$ nanostructure. (a) HAADF-STEM image. (b) Elemental profiles of Au, Ce and O acquired along the orange line indicated in (a).
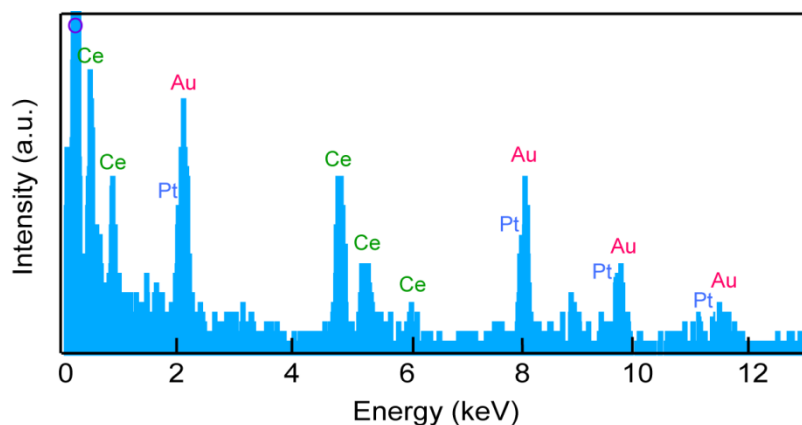
Figure S4. EDX spectrum of a representative Au/end-CeO_2 nanostructure.
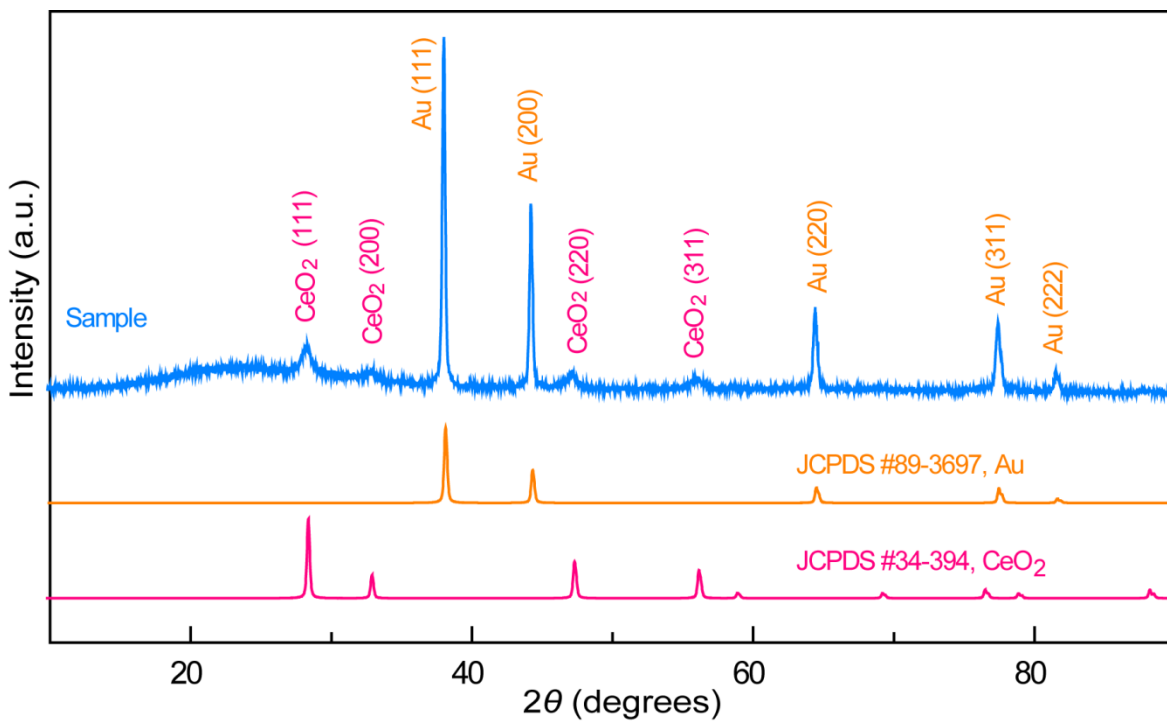
Figure S5. XRD patterns of a representative Au/end-CeO_2 nanostructure (blue). The red and orange curves are the standard powder diffraction patterns of the face-centered-cubic structure of CeO_2 (space group, F*m*-3*m*; lattice constant, 0.5411 nm) and the face-centered-cubic structure of Au (space group, F*m*-3*m*; lattice constant, 0.40796 nm).
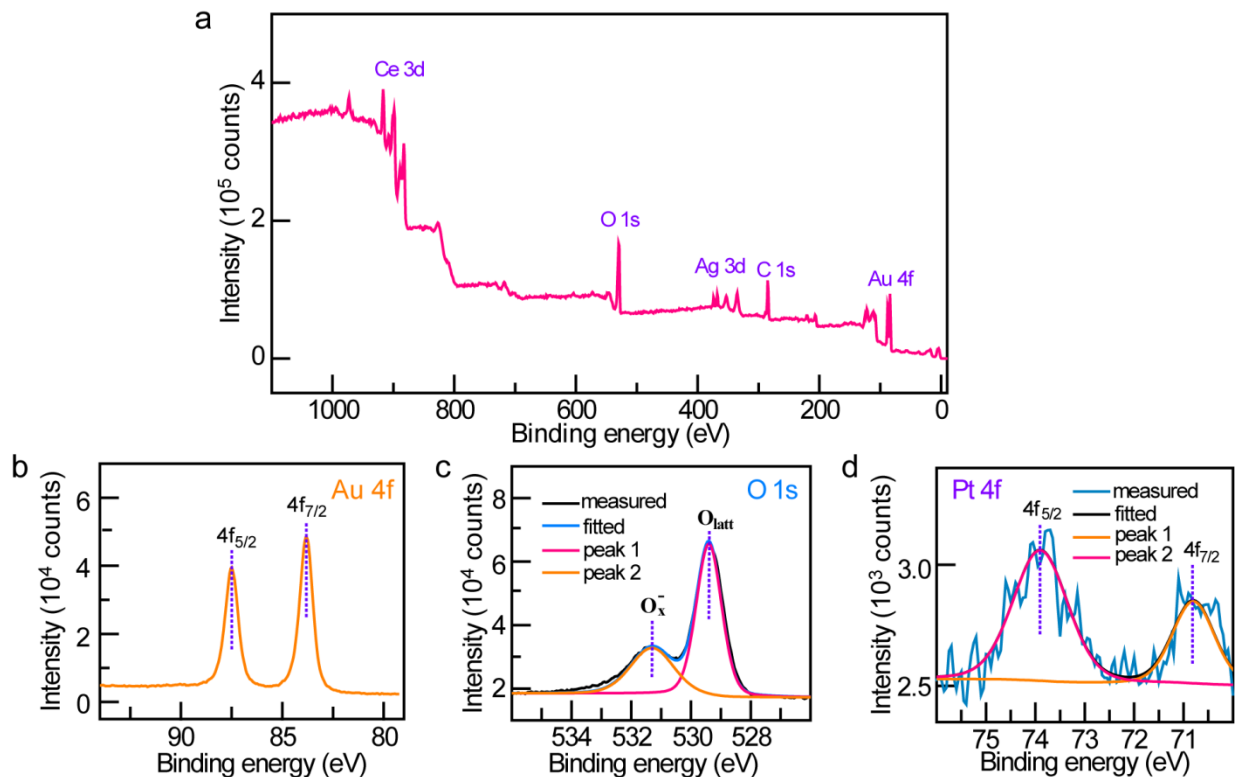
Figure S6. XPS survey spectrum (a) and high-resolution Au 4f (b), O 1s (c) and Pt 4f (d) XPS spectra of a representative Au/end-CeO$_2$ nanostructure.

The elements of Au, Ce, O, C and Ag appear on the XPS spectrum (Figure S6a). The signals of C and Ag originate from the surfactant CTAB and the shape-directing agent AgNO$_3$,[3,20] because of the exposure of side surface of the Au NRs in the nanostructures. In addition, the high-resolution Au 4f XPS spectrum (87.5 eV and 83.8 eV) suggests the metallic Au^0 state (Figure S6b). The O 1s spectrum can be fitted with two peaks (Figure S6c). Peak 1 at 529.4 eV is assigned to crystal lattice oxygen (Ce(IV)−O bond), while peak 2 at 531.3 eV is attributed to the chemisorbed water on the CeO$_2$ surface (O−H bond).[21] The binding energies of Pt 4f$_{5/2}$ (73.9 eV) and Pt 4f$_{7/2}$ (70.8 eV) are in agreement with platinum metal Pt^0 (Figure S6d).[22] The small amount of Pt element in the Au/end-CeO$_2$ sample can be verified by XPS. The Pt/Ce element ratio is calculated to be 0.00298 by integrating the peak areas of the high-resolution Pt 4f (Figure S6d) and Ce 3d (Figure 3a) XPS peaks using the Lorentzian-Gaussian function with a weight coefficient of 80%. This value is a little smaller

than that used in a typical synthesis, which is 0.004. The error is believed to come from the XPS detection method which is a surface-sensitive technique for analyzing the elemental compositions.
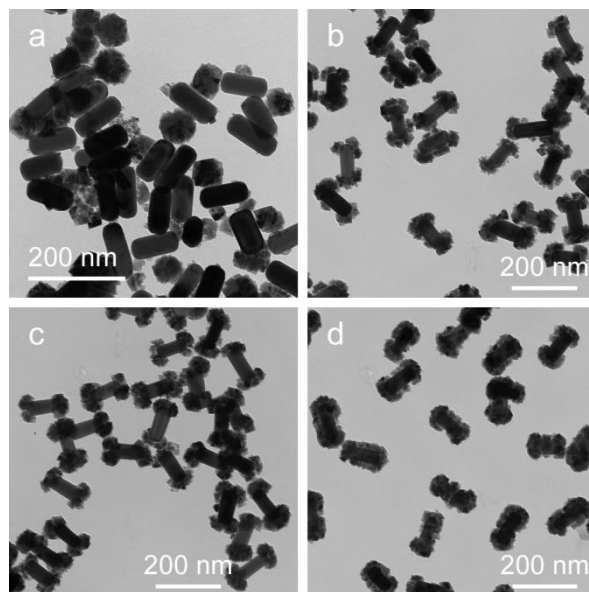
Figure S7. Effect of the amount of K_2PtCl_4 on the selective growth behavior. (a–d) Representative TEM images of the products when 0 μL (a), 50 μL (b), 200 μL (c), and 2000 μL (d) of K_2PtCl_4 solution (0.1 mM) were used, respectively.

As shown in Figure S7, without K_2PtCl_4, CeO_2 trends to self-nucleate rather than grow on the surface of the Au NRs (Figure S7a), indicating that K_2PtCl_4 is indispensable for the selective CeO_2 growth on the Au NRs. When the amount of K_2PtCl_4 is increased to 50 μL (0.1 mM), the Au/end-CeO_2 nanostructures start to form. When the amount of K_2PtCl_4 is 100−1000 μL, CeO_2 is selectively coated at the two ends of the Au NRs with a uniform morphology (Figure S7c). Further increase of K_2PtCl_4 leads to the spread of the CeO_2 shell from the two ends to the middle, and eventually the coating of the entire Au NRs when the amount is more than 2000 μL (Figure S7d). This result suggests that excess K_2PtCl_4 starts to adsorb on the side surface of the Au NRs after the adsorption is saturated on the two ends.
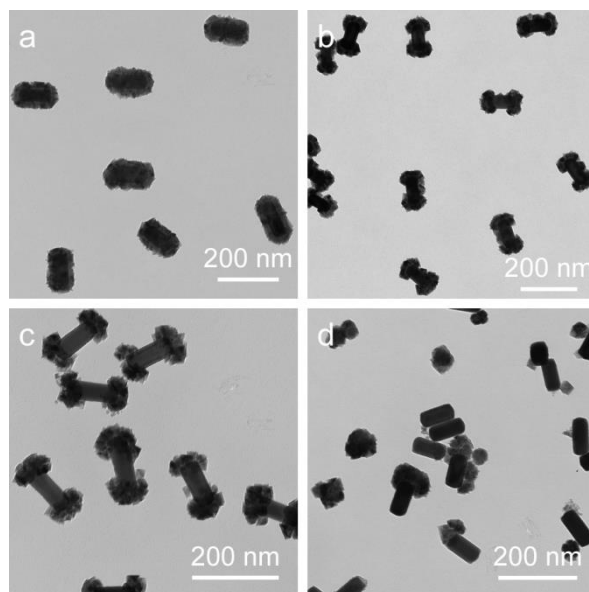
Figure S8. Effect of the CTAB concentration on the selective growth behavior. (a–d) Representative TEM images of the products when the concentration of CTAB was 5 μM (a), 20 μM (b), 50 μM (c), and 200 μM (d), respectively.

The nonuniform distribution of the CTAB molecules on the ends and side surface of Au NRs plays an important role in the preferential growth at the ends.[7,8] We further studied the effect of the CTAB concentration on the selective growth (Figure S8). When the CTAB concentration is lower than 10 μM, the core@shell nanostructures are formed (Figure S8a). When the concentration of CTAB is in the range of ~20−200 μM, the Au/end-CeO$_2$ nanostructures exist as the dominating morphology (Figure S8b,c). The further increase of the CTAB concentration makes CeO$_2$ hardly grow on the Au NRs (Figure S8d). The effect of the CTAB concentration on the CeO$_2$ growth can be understood by the hindrance of CTAB on the diffusion of PtCl$_4^{2-}$ to the Au NR surface. The lower the CTAB concentration, the less the CTAB molecules on the Au NRs and consequently the smaller hindrance on PtCl$_4^{2-}$. The PtCl$_4^{2-}$ can diffuse to the entire surface of the Au NRs, inducing the formation of the core@shell nanostructures. As the CTAB concentration increases, the amount of CTAB adsorbed on the Au NR surface increases and the hindrance to PtCl$_4^{2-}$ becomes larger. In the case of the same surface density of adsorbed CTAB at the side and ends of the Au NRs, the hindrance at the side surface is larger than that at the ends due to the smaller curvature of the side. When the CTAB concentration is very

high, the CTAB molecules adsorbed on the Au NR surface become extremely dense, which prevents $PtCl_4^{2-}$ from diffusing to the Au NR surface. As a result, it is difficult for CeO_2 to grow on the Au NRs.
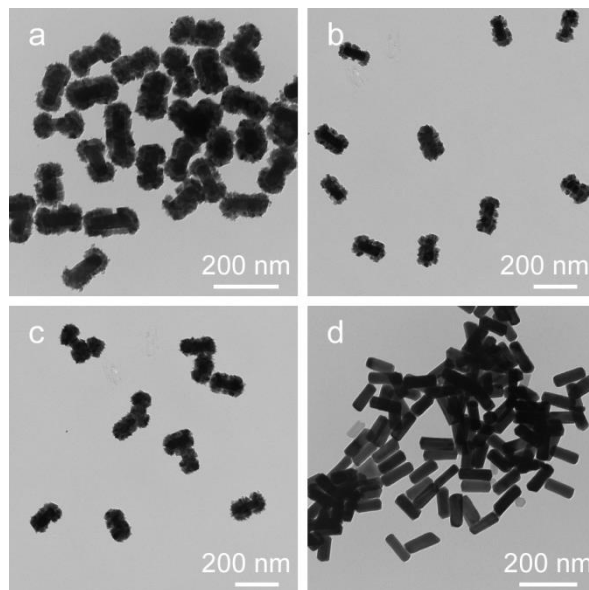

Figure S9. Control experiments. (a–c) Representative TEM images of the products grown by the replacement of K_2PtCl_4 with the same amount of H_2PtCl_6 (a), H_2PdCl_4 (b), and $AgNO_3$ (c), respectively. (d) TEM image of the product grown with $Ce(NO_3)_3$ as the ceria precursor.

Control experiments with other noble metal salts (i.e., H_2PtCl_6, H_2PdCl_4, and $AgNO_3$) as the oxidants were conducted (Figure S9a–c). The CeO_2 shells in the products have a tendency to be fully coated, suggesting that the redox potential plays an important role in the selective growth. The standard redox potentials (*vs* the standard hydrogen electrode) of the $PtCl_6^{2-}/Pt$, the $AuCl_4^-/Au$, the Ag^+/Ag, the $PtCl_4^{2-}/Pt$, and the $PdCl_4^{2-}/Pd$ redox pairs are +1.44 V,[23] +1.0 V,[24] +0.80 V,[24] +0.76 V,[25] and +0.59 V,[25] respectively. Because the redox potential of $PtCl_6^{2-}/Pt$ is much larger than that of $AuCl_4^-/Au$, $PtCl_6^{2-}$ is unsuitable for the selective coating of CeO_2 on the Au NRs through the autoredox reaction. It will result in the etching of the Au NRs. The Ag^+ ions have been reported as a good oxidant for the autoredox reaction with $Ce(OH)_3$.[26,27] However, only the core@shell nanostructures are obtained in those works because only Ag^+ ions are positively charged among the five types of ions. The positive charge makes Ag^+ ions adopt a different mechanism to induce the coating

of CeO_2 on metal nanoparticles. The redox potential of the $PdCl_4^{2-}/Pd$ is smaller than that of the $PtCl_4^{2-}/Pt$. $PdCl_4^{2-}$ has proved impractical for the selective growth of CeO_2. The smaller redox potential of the $PdCl_4^{2-}/Pd$ leads to a smaller oxidation rate for $Ce(OH)_3$, which might affect the coating kinetics of CeO_2. These results suggest that an appropriate growth rate forced by a proper redox potential difference between the oxidant and $Ce(OH)_3$ as well as an appropriate charge polarity is crucial in the selective growth of CeO_2 on the Au NRs. The $PtCl_4^{2-}/Pt$ redox pair with a reduction potential of +0.76 V proves to be the right candidate as the oxidant with $Ce(OH)_3$ for this selective growth. In addition, when $Ce(NO_3)_3$ instead of $Ce(AC)_3$ was used as the ceria precursor, no CeO_2 layer was observed on the surface of the Au NRs (Figure S9d). These results suggest that the proper precursor is also important to the selective CeO_2 coating.
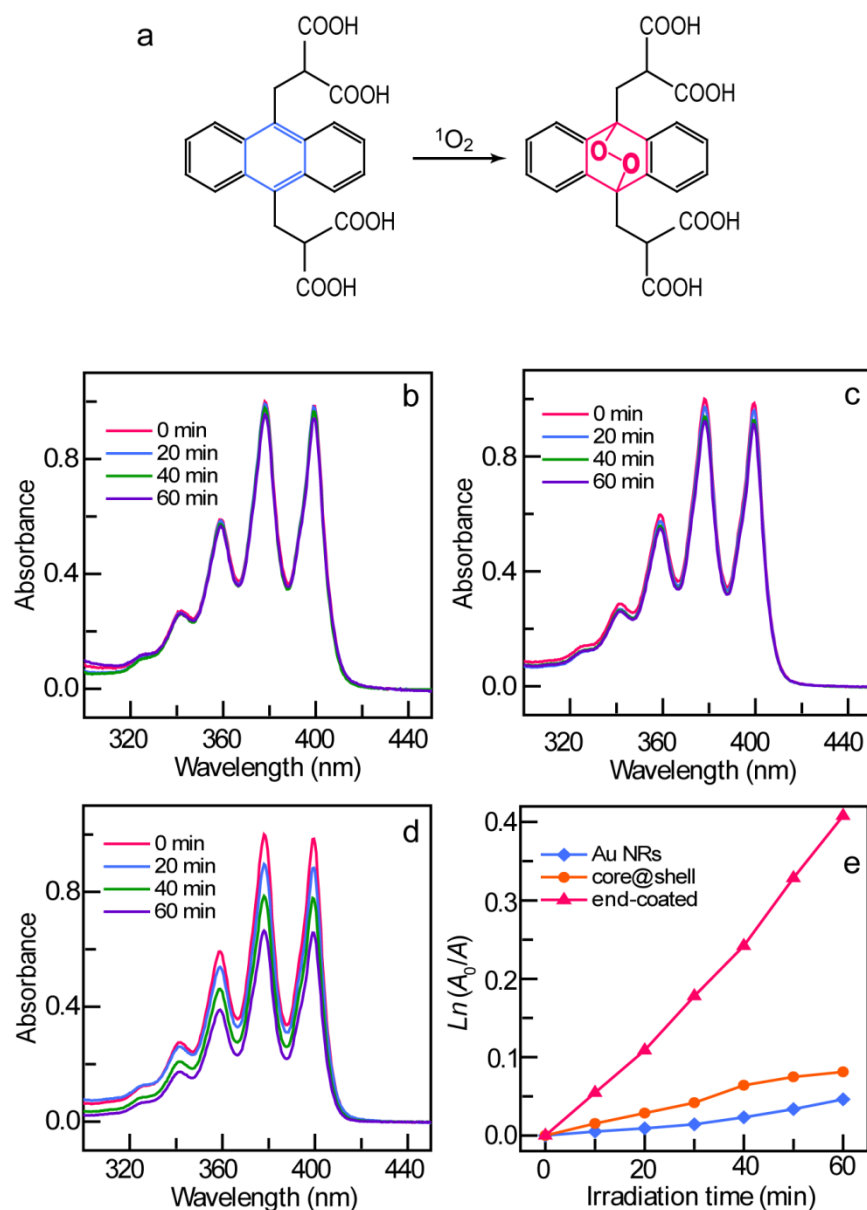
Figure S10. Singlet oxygen generation with different photocatalysts. (a) Schematic of the reaction between ABDA and $^1O_2$. (b–d) Normalized time-dependent absorption spectra of ABDA obtained with the Au NR nanostructure (b), the core@shell nanostructure (c), and the Au/end-CeO$_2$ nanostructure (d) as the photocatalysts, respectively. (e) Variance of $^1O_2$ generation rates as a function of the time with different photocatlysts under NIR illumination. The generation rate constants are calculated by assuming first-order reaction kinetics.
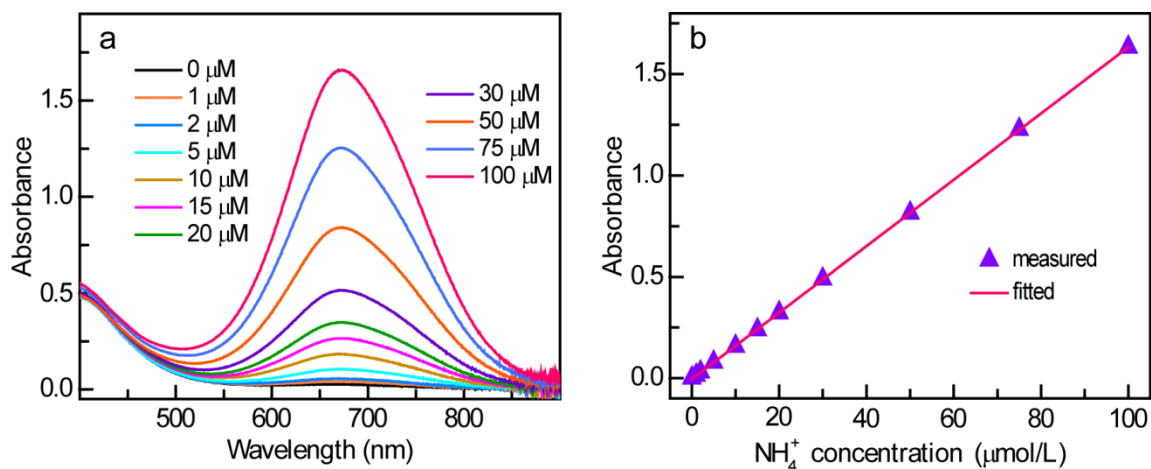
Figure S11. (a) Absorption spectra of the standard NH_4^+ solutions with different concentrations. (b) Linear calibration relationship between the absorbance value and the NH_4^+ concentration. The coefficient of determination for the linear fitting is $R^2 = 0.99998$.
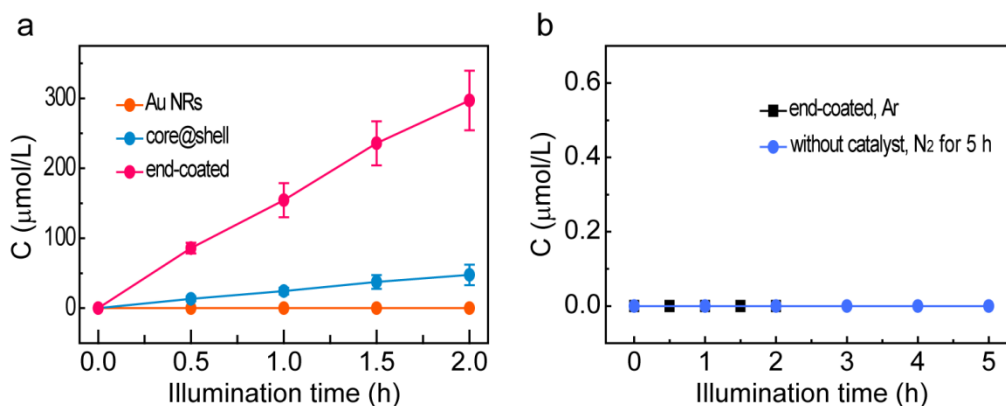
Figure S12. (a) Time-dependent ammonia generation for three types of catalysts. (b) Control experiments in Ar environment and without catalyst, respectively.

To confirm the source of ammonia, control experiments were performed. No NH_3 was detected by substituting N_2 with Ar (Figure S12b), suggesting that NH_3 was generated by the reduction of N_2. In addition, NH_3 did not come from the contamination and the impurity, because no NH_3 was detected after bubbling of N_2 under laser illumination for 5 h without the catalyst (Figure S12b).
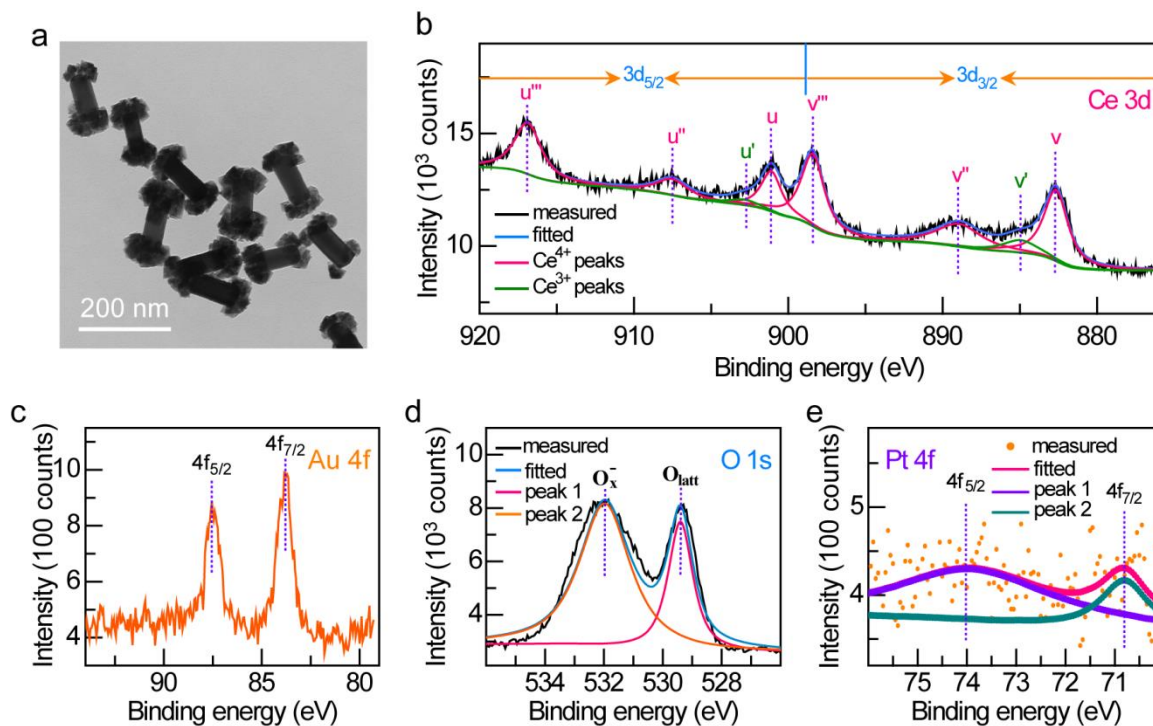
Figure S13. TEM image (a) and high-resolution Ce 3d (b), Au 4f (c), O 1s (d), and Pt 4f (e) XPS spectra of the Au/end-CeO$_2$ nanostructures after 2-h N$_2$ photofixation.

To test the stability of the Au/end-CeO$_2$ nanostructures in the N$_2$ photofixation, TEM imaging and high-resolution XPS study were conducted after 2-h photocatalysis. No significant change is observed in the morphology after 2-h photocatalysis (Figure S13a). The high-resolution Ce 3d XPS spectrum exhibits eight peaks after 2-h reaction. Six of them can be assigned to the Ce (IV) state and the other two belong to the Ce (III) state (Figure S13b). The binding energies at these peak positions are in good agreement with those before photocatalysis (Figure 3a). The Ce (IV)/Ce (III) ratio is about 90:10, a litter larger than that of the as-prepared sample. In addition, the metallic Au^0 (Figure S13c) and Pt^0 (Figure S13e) states remain unchanged. As expected, the intensity of the peak 2 in the O 1s spectrum significantly increases, which is attributed to the chemisorbed water on the CeO$_2$ surface (O–H bond) during photocatalysis. There is no significant change in the crystal lattice oxygen state.
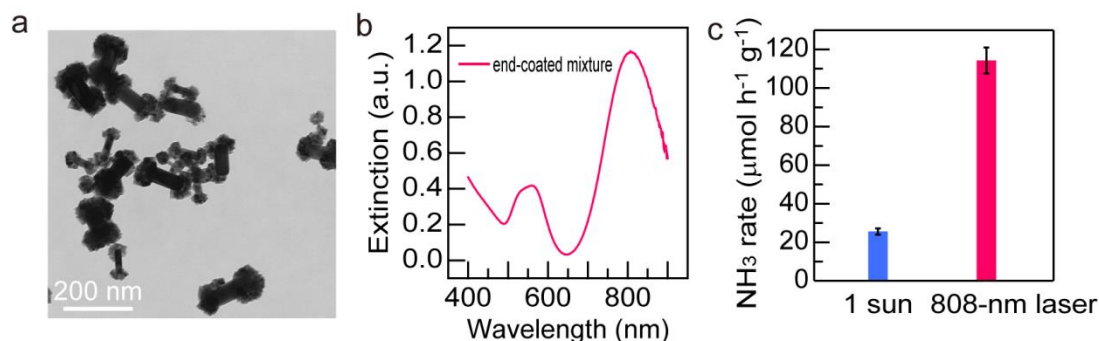
Figure S14. Plasmonic N_2 photofixation under 1 sun illumination. To improve the absorption of sunlight, three types of the Au/end-CeO_2 samples (Figure 2a–c) were mixed together at a proportion of 6:3:1. TEM image (a) and extinction spectrum (b) of three types of the Au/end-CeO_2 samples mixed at a proportion of 6:3:1. (c) Comparison of the N_2 photofixation rates under 1 sun illumination and the 808-nm laser illumination. Reaction conditions: catalyst (5.2 mg), methanol and water (2:8, v/v) mixture solution (10 mL), N_2 (15 mL·min^{-1}), and 2-h 1 sun illumination using a 500 W Xenon lamp (CEL-S500, CEAULIGHT) equipped with an AM 1.5G filter at an optical power density of 100 mW·cm^{-2}.

References

(1) Nikoobakht, B.; El-Sayed, M. A. Preparation and growth mechanism of gold nanorods (NRs) using seed-mediated growth method. *Chem. Mater.* **2003**, *15*, 1957−1962.

(2) Ni, W. H.; Kou, X. S.; Yang, Z.; Wang, J. F. Tailoring longitudinal surface plasmon wavelengths, scattering and absorption cross sections of gold nanorods. *ACS Nano* **2008**, *2*, 677−686.

(3) Chen, H. J.; Shao, L.; Li, Q.; Wang, J. F. Gold nanorods and their plasmonic properties. *Chem. Soc. Rev.* **2013**, *42*, 2679−2724.

(4) Yang, J. H.; Guo, Y. Z.; Jiang, R. B.; Qin, F.; Zhang, H.; Lu, W. Z.; Wang, J. F.; Yu, J. C. High-efficiency ″working-in-tandem″ nitrogen photofixation achieved by assembling plasmonic gold nanocrystals on ultrathin titania nanosheets. *J. Am. Chem. Soc.* **2018**, *140*, 8497−8508.

(5) Zhu, D.; Zhang, L. H.; Ruther. R. E.; Hamers, R. J. Photo-illuminated diamond as a solid-state source of solvated electrons in water for nitrogen reduction. *Nat. Mater.* **2013**, *12*, 836−841.

(6) Kou, X. S.; Sun, Z. H.; Yang, Z.; Chen, H. J.; Wang, J. F. Curvature-directed assembly of gold nanocubes, nanobranches, and nanospheres. *Langmuir* **2009**, *25*, 1692−1698.

(7) Wu, B. H.; Liu, D. Y.; Mubeen, S.; Chuong, T. T.; Moskovits, M.; Stucky, G. D. Anisotropic growth of TiO_2 onto gold nanorods for plasmon-enhanced hydrogen production from water reduction. *J. Am. Chem. Soc.* **2016**, *138*, 1114−1117.

(8) Wang, F.; Cheng, S.; Bao, Z. H.; Wang, J. F. Anisotropic overgrowth of metal heterostructures induced by a site-selective silica coating. *Angew. Chem., Int. Ed.* **2013**, *52*, 10344−10348.

(9) Caswell, K. K.; Wilson, J. N.; Bunz, U. H. F.; Murphy, C. J. Preferential end-to-end assembly of gold nanorods by biotin−streptavidin connectors. *J. Am. Chem. Soc.* **2003**, *125*, 13914−13915.

(10) Zheng, Z. K.; Tachikawa, T.; Majima, T. Single-particle study of Pt-modified Au nanorods for plasmon-enhanced hydrogen generation in visible to near-infrared region. *J. Am. Chem. Soc.* **2014**, *136*, 6870−6873.

(11) Pérez-Juste, J.; Liz-Marzán, L. M.; Carnie, S.; Chan, D. Y. C.; Mulvaney, P. Electric-field-directed growth of gold nanorods in aqueous surfactant solutions. *Adv. Funct. Mater.* **2004**, *14*, 571−579.

(12) Rodríguez-Fernández, J.; Pérez-Juste, J.; Mulvaney, P.; Liz-Marzán, L. M. Spatially-directed oxidation of gold nanoparticles by Au (III)−CTAB complexes. *J. Phys. Chem. B* **2005**, *109*, 14257−14261.

(13) Wang, Z. L.; Mohamed, M. B.; Link, S.; El-Sayed, M. A. Crystallographic facets and shapes of gold nanorods of different aspect ratios. *Surf. Sci.* **1999**, *440*, L809−L814.

(14) Wang, Z. L.; Gao, R. P.; Nikoobakht, B.; El-Sayed, M. A. Surface reconstruction of the unstable {110} surface in gold nanorods. *J. Phys. Chem. B* **2000**, *104*, 5417−5420.

(15) Nikoobakht, B.; El-Sayed, M. A. Evidence for bilayer assembly of cationic surfactants on the surface of gold nanorods. *Langmuir* **2001**, *17*, 6368−6374.

(16) Johnson, C. J.; Dujardin, E.; Davis, S. A.; Murphy, C. J.; Mann, S. Growth and form of gold nanorods prepared by seed-mediated, surfactant-directed synthesis. *J. Mater. Chem.* **2002**, *12*, 1765−1770.

(17) Nie, Z. H.; Fava, D.; Rubinstein, M.; Kumacheva, E. ″Supramolecular″ assembly of gold nanorods end-terminted with polymer ″pom-poms″: effect of pom-pom structure on the association modes. *J. Am. Chem. Soc.* **2008**, *130*, 3683−3689.

(18) Carbó-Argibay, E.; Rodríguez-González, B.; Gómez-Graña, S.; Guerrero-Martínez, A.; Pastoriza-Santos, I.; Pérez-Juste, J.; Liz-Marzán, L. M. The crystalline structure of gold nanorods revisited: evidence for higher-index lateral facets. *Angew. Chem., Int. Ed.* **2010**, *49*, 9397−9400.

(19) Grzelczak, M.; Pérez-Juste, J.; Rodríguez-González, B.; Liz-Marzán, L. M. Influence of silver ions on the growth mode of platinum on gold nanorods. *J. Mater. Chem.* **2006**, *16*, 3946−3951.

(20) Liz-Marzán, L. M.; Grzelczak, M. Growing anisotropic crystals at the nanoscale. *Science* **2017**, *356*, 1120−1121.

(21) Li, B. X.; Gu, T.; Ming, T.; Wang, J. X.; Wang, P.; Wang, J. F.; Yu, J. C. (Gold core)@(ceria shell) nanostructures for plasmon-enhanced catalytic reactions under visible light. *ACS Nano* **2014**, *8*, 8152−8162.

(22) Liu, X.; Chen, N.; Han, B. Q.; Xiao, X. C.; Chen, G.; Djerdj, I.; Wang, Y. D. Nanoparticle cluster gas sensor: Pt activated SnO_2 nanoparticles for NH_3 detection with ultrahigh sensitivity. *Nanoscale* **2015**, *7*, 14872−14880.

(23) Tsuji, M.; Hamasaki, M.; Yajima, A.; Hattori, M.; Tsuji, T.; Kawazumi, H. Synthesis of Pt−Ag alloy triangular nanoframes by galvanic replacement reactions followed by saturated NaCl treatment in an aqueous solution. *Mater. Lett.* **2014**, *121*, 113−117.

(24) Gilroy, K. D.; Ruditskiy, A.; Peng, H.-C.; Qin, D.; Xia, Y. N. Bimetallic nanocrystals: syntheses, properties, and applications. *Chem. Rev.* **2016**, *116*, 10414−10472.

(25) Skrabalak, S. E.; Chen, J. Y.; Sun, Y. G.; Lu, X. M.; Au, L.; Cobley, C. M.; Xia, Y. N. Gold nanocages: synthesis, properties, and applications. *Acc. Chem. Res.* **2008**, *41*, 1587−1595.

(26) Mitsudome, T.; Mikami, Y.; Matoba, M.; Mizugaki, T.; Jitsukawa, K.; Kaneda, K. Design of a silver−cerium dioxide core−shell nanocomposite catalyst for chemoselective reduction reactions. *Angew. Chem., Int. Ed.* **2012**, *51*, 136−139.

(27) Song, S. Y.; Li, K.; Pan, J.; Wang, F.; Li, J. Q.; Feng, J.; Yao, S.; Ge, X.; Wang, X.; Zhang, H. J. Achieving the trade-off between selectivity and activity in semihydrogenation of alkynes by fabrication of (asymmetrical Pd@Ag core)@(CeO_2 shell) nanocatalysts via autoredox reaction. *Adv. Mater.* **2017**, *29*, 1605332.